Probing the Functional Heterogeneity of Surface Binding Sites by Analysis of Experimental Binding Traces and the Effect of Mass Transport Limitation

Juraj Svitel,* Hacène Boukari,† Donald Van Ryk,* Richard C. Willson,‡ and Peter Schuck*

*National Institute of Biomedical Imaging and Bioengineering, National Institutes of Health, Bethesda, Maryland; †Laboratory of Integrative and Medical Biophysics, National Institute of Child Health and Human Development, National Institutes of Health, Bethesda, Maryland; and ‡Departments of Chemical Engineering and of Biology & Biochemistry, University of Houston, Houston, Texas

ABSTRACT Many techniques rely on the binding activity of surface-immobilized proteins, including antibody-based affinity biosensors for the detection of analytes, immunoassays, protein arrays, and surface plasmon resonance biosensors for the study of thermodynamic and kinetic aspects of protein interactions. To study the functional homogeneity of the surface sites and to characterize their binding properties, we have recently proposed a computational tool to determine the distribution of affinity and kinetic rate constants from surface binding progress curves. It is based on modeling the experimentally measured binding signal as a superposition of signals from binding to sites spanning a range of rate and equilibrium constants, with regularization providing the most parsimonious distribution consistent with the data. In the present work, we have expanded the scope of this approach to include a compartment-like transport step, which can describe competitive binding to different surface sites in a zone of depleted analyte close to the sensor surface. This approach addresses a major difficulty in the analysis of surface binding where both transport limitation as well as unknown surface site heterogeneity may be present. In addition to the kinetic binding parameters of the ensemble of surface sites, it can provide estimates for effective transport rate constants. Using antibody-antigen interactions as experimental model systems, we studied the effects of the immobilization matrix and of the analyte flow-rate on the effective transport rate constant. Both were experimentally observed to influence mass transport. The approximate description of mass transport by a compartment model becomes critical when applied to strongly transport-controlled data, and we examined the limitations of this model. In the presence of only moderate mass transport limitation the compartment model provides a good description, but this approximation breaks down for strongly transport-limited surface binding. In the latter regime, we report experimental evidence for the formation of gradients within the sensing volume of the evanescent field biosensor used.

INTRODUCTION

When studying the binding of macromolecules to surfaces, it can be desirable to consider heterogeneity of the surface binding sites (1–4). This question can arise, for example, when studying the interactions of a soluble protein species with surface-immobilized binding partners, where the surface sites may either be intrinsically inhomogeneous in their binding properties, or may be rendered heterogeneous by attaching them to the surface. Protein samples that form chemically heterogeneous ensembles, for example, due to variability in the amino-acid sequence, differential glycosylation, or other post-translational modifications may exhibit heterogeneous binding properties. An example of great immunological interest, historically as well as in current biotechnological applications, is the characterization of polyclonal antibodies (5,6) . Immobilization of chemically homogeneous protein species frequently results in functionally impaired subpopulations, due to constraints in orientation, variable chemical crosslinking, or influence of the microenvironment of the surface (7–9). This can greatly affect applications ranging from antibody-based affinity biosensors and protein arrays (1,10,11), to the study of protein interactions by surface plasmon resonance (SPR) biosensors (12–14). Protein surface immobilization with chemically uniform attachment and high activity to surfaces with a low degree of nonspecific binding is a very active area of research.

Evanescent field biosensors have become popular tools in the characterization of protein-protein, protein-small molecule, protein-nucleic acid interactions, and DNA hybridization, as well as multiprotein complexes (15–17). They allow kinetic binding traces to be measured with high sensitivity and remarkable reproducibility, yet strikingly few experimental applications have resulted in binding kinetics consistent with the ideal binding progress of a simple 1:1 interaction (18–21). Interpreting these deviations as a source of information on the homogeneity of the surface-immobilized sites, we have recently proposed a new computational model that assumes the binding signal to be a superposition of independent parallel binding reactions with a continuous distribution of thermodynamic and kinetic binding constants (22). This was motivated by the point of view that it cannot be assumed that only one or a few discrete classes of surface binding sites exist. Instead, a priori a continuum of binding energies may be possible, considering the complexity of the

Submitted August 2, 2006, and accepted for publication November 16, 2006.

Address reprint requests to Dr. P. Schuck, Tel.: 301-435-1950; E-mail: pschuck@helix.nih.gov.

J. Svitel's present address is Amgen, Inc., Thousand Oaks, CA 91320.

D. Van Ryk's present address is Laboratory of Immunoregulation, NIAID, National Institutes of Health, Bethesda, Maryland, MD 20892.

0006-3495/07/03/1742/17 $2.00

doi: 10.1529/biophysj.106.094615

surface properties, its microenvironment, and protein immobilization and conformation. With a suitable set of experimental binding progress curves measured at different analyte concentrations, this method can be used to characterize the populations of different classes of surface sites from a functional perspective with regard to the binding activity for a soluble ligand (22).

In this work, we aimed at expanding the scope of this method to include first-order corrections for mass transport influence. Mass transport limitation has long been recognized as another major difficulty in kinetic surface binding experiments in many experimental systems (23–25). Depending on the experimental configuration, the diffusion and/or flow from the bulk to the sensor surface, or hindered diffusion and nonspecific binding within a polymeric immobilization matrix, may limit the surface binding for fast chemical kinetics (14,26). This leads to the formation of a depletion zone of analyte close to the surface sites. Using a novel compartment model for a transport step to the vicinity of heterogeneous surface sites, we show in this article that estimates for both the distribution of surface sites and for a single overall transport rate constant can be obtained from modeling sets of experimental binding progress curves, leading to a fit of experimental data to within close to the noise of data acquisition. This approach can be used to characterize the immobilized surface sites of interest, as well as to visualize the populations of sites with impaired binding activity.

Since the approach reports the transport rate constant for mass transport limited binding, it also offers the potential to study the transport process itself. Consequently, we have studied possible factors contributing to mass transport limitation, such as flow-rate and the size of the immobilization matrix. Obviously, for completely mass transport-limited surface binding no information on the chemical binding rate constants of the surface sites can be expected, thus limiting the potential application of the approach to the experimental regime where the surface binding is influenced by both chemical kinetics and mass transport. While this regime is of great practical importance, we finally experimentally explored the case when the compartment-like transport approximation ceases to be applicable.

METHODS

Data analysis in the absence of mass transport limitations

In the absence of mass transport limitation, the computational approach reported previously (22) was used for estimating the rate and affinity distributions. In brief, sets of kinetic traces were fitted from an association phase, where at initial time, t_0, an analyte at concentration c is brought in contact with the sensor surface for a duration t_c, and the dissociation phase where the analyte is removed from the vicinity of the sensor surface. The binding signal $s(t)$ from several traces at different analyte concentrations were fitted with a model considering a continuous distribution of binding sites $P(k_{off}, K_D)$ with a range of chemical off-rate constants k_{off} and equilibrium dissociation constants K_D. In this model, $P(k^*_{off}, K^*_D)\, dk_{off}\, dK_D$ is the population of the class of surface sites (in signal units) with an off-rate constant k^*_{off} and the equilibrium constant K^*_D. In the absence of transport limitation, binding to each class of sites is assumed to proceed independently with the following pseudo-first-order rate equation

$$\frac{ds}{dt} = k_{on}c(S - s) - k_{off}s, \tag{1}$$

where k_{on} is the chemical on-rate constant with $k_{on} = k_{off}/K_D$, and S is the saturating signal for this class of sites. The analytical solution of Eq. 1 consists of well-known sets of exponentials, normalized to $S = 1$, which follow:

$$s_1(k_{off}, K_D, c, t) = (1 + K_D/c)^{-1} \times \begin{cases} 1 - e^{-(k_{on}c + k_{off})(t - t_0)} & t_0 < t \le t_0 + t_c \\ [1 - e^{-(k_{on}c + k_{off})(t_c - t_0)}]e^{-k_{off}(t - t_c)} & t > t_0 + t_c \end{cases}. \tag{2}$$

Since we have a distribution of binding sites, the total measured signal, s_{tot}, can be expressed as a Fredholm integral equation

$$s_{tot}(c, t) = \int_{K_{D,min}}^{K_{D,max}} \int_{k_{off,min}}^{k_{off,max}} s(k_{off}, K_D, c, t)P(k_{off}, K_D)dk_{off}dK_D, \tag{3}$$

which can be discretized in a grid of ($k_{off,i}$, $K_{D,i}$) values

$$s_{tot}(c, t) = \sum_{i=1}^{N} P_i(k_{off,i}, K_{D,i})s(k_{off,i}, K_{D,i}, c, t)\Delta k_{off}\Delta K_D \tag{4}$$

(with the index i enumerating all surface species with associated pairs of (k_{off}, K_D) values from 1 to N) and solved to give the distribution $P_i(k_{off,i}\, K_{D,i})$ of surface binding sites. To avoid instabilities, Tikhonov regularization was used (27), following an approach outlined by Provencher (28), which was applied previously also in the computation of adsorption energy distributions in the literature (29,30). We compute the most parsimonious distribution that fits the experimental data within a statistical confidence level of between one and two standard deviations. By design, regularization introduces a bias in the results, but one that is consistent with the principle of Occam's razor. The extent of bias can be assessed, in principle, by changing the scaling parameter for the regularization (i.e., the preassigned confidence level), switching regularization off, or changing the regularization method. The latter approach was not implemented.

In practice, Eqs. 2 and 4 are modified to take into account baseline offsets for the kinetic traces at each analyte concentration in the presence and absence of analyte, respectively. Since the effective start time t_0 of the binding experiments are not precisely known (due to instrumental and flow-based delays), t_0 times are also included as fitting parameters for each curve, within the bounds of the experimental uncertainty. Further, a factor describing a uniform fractional decay of the surface sites after each round of regeneration, similar to that described first by Ober (31), can be introduced in Eq. 2 and modeled to the data.

We have verified that the distributions $P(k_{off}, K_D)$ calculated with different discretization of the k_{off}–K_D space converge with sequentially finer grids, with little improvement beyond approximately three to four divisions per decade in both parameters. To avoid the distribution extending into the range of binding constants that cannot be experimentally observed, such as unpopulated low affinity sites (high k_{off} and K_D), or binding that cannot be distinguished from a baseline offset (very low k_{off} and K_D), a series of fits with different ranges of k_{off} and K_D values was performed, and the smallest range of k_{off} and K_D was chosen that provided an acceptable fit, as assessed by the root mean-square deviation (RMSD). However, when significant peaks of the distribution occurred at the limits of the K_D or k_{off} range, this model was rejected and the distribution range was extended.

Transport-limited binding to distributions of surface sites

A two-compartment model considers binding influenced by limited transport of analyte from a bulk compartment (at concentration c_0) to a hypothetical compartment at the surface (at concentration c_s). In this first approximation for transport, each compartment is assumed to be internally well mixed. In this highly simplified description of transport, all consideration of the spatial distribution and spatial inhomogeneities are being ignored, other than the abstract designation for the analyte to be either ''far from'' or ''close to'' the surface binding sites. Although this concept clearly cannot be expected to account, for example, for coupled reaction-diffusion processes, it has been used successfully as a first approximation to describe, with a single rate equation, the effect of transport on chemical reaction kinetics where the transport and binding can be considered to proceed sequentially and independently (14,23,32).

If the partial contribution to the total signal from sites with binding constants $k_{on,i}$ and $k_{off,i}$ is denoted as s_i, with a total number of N sites considered, the rate equations for all classes of binding sites can be written as

$$\frac{ds_i}{dt} = k_{on,i}c_s(s_{max,i} - s_i) - k_{off,i}s_i \quad \text{for all } i$$
$$\frac{dc_s}{dt} = k_{tr}(c_0 - c_s) - \sum_{j=1}^{N}\frac{ds_j}{dt}, \tag{5}$$

(with the transport rate constant k_{tr} in units of s^{-1}, and the signals s_i in units of volume concentration in the surface compartment). For modeling transport-limited binding to a distribution of surface sites, the strategy is to chose a large ensemble of sites i that represent grid points of a discretized representation of a continuous k_{off}-K_D-surface, such that the set of calculated s_i values becomes a distribution analogous to the P_i ($k_{off,i}$, $K_{D,i}$) introduced above for the non-transport-limited case (Eq. 4). An important difference is that in the transport-limited case the binding to the individual sites becomes coupled (in contrast to the independent summation in Eq. 4), a fact that arises from the competition of all sites for the analyte in the compartment close to the surface.

It can be shown that assuming laminar flow in a channel above the sensor surface, the transport rate constant k_{tr} depends on the diffusion coefficient D of the analyte approximately as

$$k_{tr} \approx 1.282(v)^{1/3}(hl)^{-1/3}D^{2/3}, \tag{6}$$

where v is the flow rate, and h and l the height and length of the flow channel above the sensor surface, respectively (33). For example, for the flow cell dimensions in the Biacore 3000 instrument (Biacore, Piscataway, NJ), when the conversion 1 RU $\sim$ 1 pg/mm^2 is used (18,34), we arrive at an apparent diffusion coefficient of $D \approx 3.38 \times 10^{-10}[k_{tr}/(\text{RU/Ms})]^{3/2} \times [\text{M/kDa}]^{-3/2} \times [v/(\mu\text{l/min})]^{-1/2} \times 10^{-7}\text{cm}^2/\text{s}$.

In this compartment model, after a fast transition period, dc_s/dt becomes much smaller than $\Sigma ds_i/dt$, and under these steady-state conditions, the surface concentration can be approximately solved as

$$c_s = c_0 - \frac{1}{k_{tr}}\sum_{j=1}^{N}\frac{ds_j}{dt}, \tag{7}$$

which leads to the rate of surface binding to each site

$$\frac{ds_i}{dt} = k_{on,i}c_0(s_{max,i} - s_i) - k_{off,i}s_i - \frac{k_{on,i}(s_{max,i} - s_i)}{k_{tr}}\sum_{j=1}^{N}\frac{ds_j}{dt}, \tag{8}$$

with the third term approximating the effect of transport limitation. Compared to the standard form Eq. 1, the rate equations for all sites are coupled due to their competition for the analyte in the surface compartment. This competition takes place both in the transport-limited association phase as well as during rebinding in the dissociation phase. Also, the extent of competition depends on the particular distribution of sites P_i, which consists of the set of saturating signals $s_{max,i}$ for each site with ($k_{off,i}$, $K_{D,i}$).

Given any particular distribution $P_i(k_{off,i}, K_{D,i})$, Eq. 8 was solved using the Cash-Karp Runge-Kutta method (35). To improve the computational time, the square grid of (k_{off}, K_D) values between $k_{off,min}$, $k_{off,max}$, $K_{D,min}$, and $K_{D,max}$ was truncated by additionally imposing upper and lower limits on k_{on}. Optimization of the distribution to fit the experimentally measured traces was achieved with the Levenberg-Marquardt method as implemented in MATLAB (The MathWorks, Natick, MA). (All MATLAB code and .dll executables used in the present work are available upon request.) For some stages of the optimization, the baseline parameters were computed analytically for each distribution, following the principle of separation of linear and nonlinear parameters (36). The best-fit transport rate constant k_{tr} was determined initially by mapping the best-fit RMSD as a function of k_{tr}, followed by fine adjustment through nonlinear least-squares optimization jointly with the distribution. After determining the best-fit k_{tr} and its associated RMSD, the distribution P_i was optimized with maximum entropy regularization, scaled to achieve a relative increase in the RMSD of the fit as determined by F-statistics on a confidence level of 0.9.

For global modeling of experimental binding traces at different concentrations and different analyte flow rates from the same sensor surface, the global RMSD was optimized, treating individual k_{tr} values as local parameters for each set of traces at one particular flow rate, and treating the distribution of surface sites P_i as a global parameter common to all traces.

EXPERIMENTAL

Biosensor experiments

As one model system, a mouse monoclonal IgG specific against human β_2-microglobulin (Biacore, lot No. 1130624) was surface immobilized, and β_2-microglobulin (Biacore, and Sigma-Aldrich, St. Louis, MO) was used as an analyte. Surface plasmon resonance biosensor experiments with flow-injections were performed using a Biacore 3000 instrument (Biacore). The flow channel in the Biacore 3000 has a height of 0.02 mm and a length of 2.4 mm (37,38). Flow rates between 1 and 50 μl/min were used as indicated. Sensor chips F1 containing a ''short'' matrix of carboxymethylated dextran (we believe at present termed CM3), and chips CM5 containing a ''long'' (100–200 nm) carboxymethylated dextran matrix were used. The ''short'' matrix is thought to have a height of only 30–40% compared to a CM5 surface (39). Where practical, contact times were chosen to provide information on the plateau region of steady-state binding, and sets of analyte concentrations were used to cover at least the range from 0.1-fold to 10-fold of the anticipated equilibrium dissociation constant.

The antibody was immobilized by standard amine coupling as described elsewhere (40,41). In brief, the surface was activated for 7 min with a mixture of 500 mM n-hydroxysuccinimide and 200 mM n-ethyl-n'-(3-dimethylaminopropyl)-carbodiimide, followed by surface exposure of the ligand in 10 mM sodium acetate pH 5.5, and deactivation with 1 M ethanolamine. Binding experiments were conducted with the running buffer 10 mM HEPES, 150 mM NaCl, 3 mM EDTA, 0.005% v/v surfactant P20 at pH 7.4 at 25°C. No chemical regeneration was necessary, since virtually complete dissociation can be achieved after a few hours. Before the first use, the surface was stabilized by five consecutive cycles of saturation and complete dissociation, and a constant saturation signal was attained usually after the first cycle. SPR signals from a blank surface in series with the functionalized surface were collected and subtracted from the signal to eliminate bulk refractive index contributions and some possible nonspecific binding to the sensor surface (42). The signal from the blank surface was typically $\sim$10–20 RU. The sensor signal was converted to mass per surface area using the conversion constant of 1 RU per 10^{-6} refractive index units, or 1 pg/mm^2 (18,34).

The experiments under virtually complete mass transport control were conducted on a Biacore X instrument. Hen egg lysozyme (HEL) was purchased from Worthington (Lakewood, NJ), and HyHel-10 was prepared as

described in Xavier and Willson (43). The anti-HEL mAb surfaces were regenerated with glycine pH 2.0–2.05.

Fluorescence correlation spectroscopy

Fluorescence correlation spectroscopy (FCS) measures the intensity-intensity correlation function (44–46)

$$F(\tau) = 1 + \frac{\langle \delta I(t)\delta I(t+\tau)\rangle}{\langle I(t)\rangle^2}, \quad (9)$$

where $\delta I(t) = I(t) - \langle I(t)\rangle$ denotes the deviation of the fluorescent intensity, $I(t)$, measured at time, t, from the time-average intensity, $\langle I(t)\rangle$. Typically, the measured intensity is related to the number of fluorescent particles moving in and out of a small illuminated volume. For freely diffusing particles, a closed form expression for Eq. 9 was derived (47)

$$F(\tau) = 1 + \frac{1}{\overline{N}} \frac{1}{(1+\tau/\tau_d)(1+p\tau/\tau_d)^{1/2}}, \quad (10)$$

where $\overline{N}$ is related to the average number of particles in the detected volume and τ_d the diffusion time. In the derivation of Eq. 10 the intensity profile of the illuminated volume is assumed to be a three-dimensional Gaussian ($\sim\exp(-2\,(r/r_0)^2)\exp(-2(z/z_0)^2)$), characterized by two length scales, r_0, and z_0, defined in the focusing plane and the optical axis along the direction of the beam, respectively. In Eq. 10, $p = (r_0/z_0)^2$ is an instrumental constant and $\tau_d = (r_0)^2/4D$, D being the translational diffusion coefficient of the fluorescent particle.

FCS provides the ability to detect and follow the dynamics of fluorescent particles in a nonfluorescent crowded environment such as concentrated polymer solutions (48). This was exploited to study the diffusion of fluorescently labeled β_2-microglobulin (0.26 Alexa/protein) in carboxymethylated (CM) dextran solutions. The CM dextran (500 kDa) was a generous gift of Dr. Erk Gedig (XanTec, Muenster, Germany). Both components were dissolved in PBS buffer and several samples were prepared with various dextran concentrations but with fixed, low concentration of β_2-microglobulin concentration ($\sim$100 nM). All FCS data were collected at $T = 25$°C.

Details on our custom-built FCS setup have been described elsewhere (49). FCS correlation functions were collected and analyzed to extract mainly the diffusion coefficient of β_2-microglobulin as a function of the dextran concentration. We found that the expression in Eq. 10 described well the experimental data, suggesting that the fluorescent protein is highly monodisperse in size. Further, analysis of the amplitude of the correlation function (the limiting value $F(\tau > 0)$) indicated no observable oligomerization of β_2-microglobulin when dextran is added.

RESULTS

First, to illustrate the utility of the surface-site distribution analysis, Fig. 1 *A* shows the kinetic traces of β_2-microglobulin binding to a ''short'' carboxymethylated dextran surface functionalized by amine coupling of a monoclonal IgG. On this surface, at the relatively high flow rate (20 μl/min) and low total surface density of sites (100 pg/mm^2), we did not observe significant effects of mass transport limitation. The binding curves are typical for most observed with SPR biosensors in that they are very reproducible, but cannot be satisfactorily modeled assuming the presence of one class of surface sites (*thin short dashed line*). A single-site model cannot fit well the continued increase in signal at the highest concentration, and systematically deviates in the dissociation kinetics. The residuals of such a fit are shown in Fig. 1 *B* (RMS error 1.18 RU). The ad hoc assumption of two classes of surface sites leads to a better fit (Fig. 1 *C*, RMS error 0.56 RU). With the model that there can be many classes of surface sites with a continuous distribution of thermodynamic and kinetic binding constants, we obtain a fit close to the noise of the data acquisition (Fig. 1 *A*, *bold dashed line*, residuals in Fig. 1 *D*, RMS error 0.31 RU). The best-fit estimate of the affinity and rate constant distribution (Fig. 1 *E*) exhibits a main peak with signal-average $K_D \sim 1.7$ nM (average $k_{off} \sim 1.8 \times 10^{-3}$/s) and a smaller peak at $\sim$100

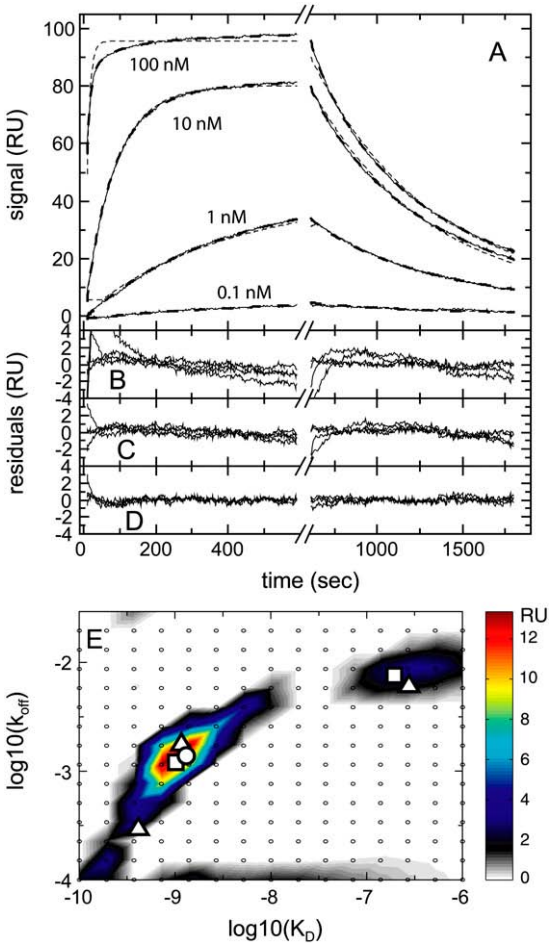

FIGURE 1 Properties of the surface site distribution in the absence of transport limitation. (*A*) Binding progress of soluble β_2-microglobulin to a monoclonal IgG immobilized to a carboxymethylated dextran surface (F1 chip). Analyte concentrations: 0.1, 1, 10, and 100 nM. Experimental curves (*solid lines*), best-fit curves using the surface site distribution model (*bold long dashed lines*), and best-fit curves from a single-site model (*thin short dashed lines*). (*B*) The single-site model results in a best-fit $K_D = 1.35$ nM and $k_{off} = 1.4 \times 10^{-3}$/s with an RMS error of 1.18 RU. (*C*) The two-site model converges to $K_{D,1} = 1.03$ nM and $K_{D,2} = 200$ nM with an RMS error 0.56 RU. (*D*) Residuals of the distribution model with an RMS error of 0.31 RU. (*E*) Affinity and rate-constant distribution calculated on a grid of K_D and k_{off} value as indicated by the small circles, with the interpolated distribution values indicated by the colored contour plot. Results of the discrete site models are indicated by symbols: single-site (*circle*), two-site (*squares*), and three-site (*triangles*).

nM–1 μM (accounting for 17% of the surface sites), and in addition a small fraction of surface sites with low k_{off}.

Comparing the continuous distribution model with the two-site model that represents both peaks but describes them as uniform classes of sites, the fit improves by almost a factor of two. This suggests that the surface sites may not be homogeneous, but exhibit microheterogeneity in affinity. Although the model of a continuous K_D-k_{off} distribution does clearly show a main peak in affinity that is stretched from ~0.5 to 3 nM, a more precise assessment of the populations of sites does not seem possible. Due to the limited information content of the noisy exponentials, the detailed decomposition into subpopulations of sites is an ill-posed problem. To avoid overinterpretation, we have applied the strategy of regularization, which provides the broadest and smoothest distribution consistent with the data (28,50). By design, regularization introduces bias by selecting the most parsimonious distribution among all distributions that fit the data statistically indistinguishably well. This approach is routinely used in other fields, including dynamic light scattering (51) and sedimentation velocity ultracentrifugation (52), and its advantages as well as limitations have been well studied. For the current analysis, we found that the main peak was consistently well determined (Fig. 1 *E*). While the smaller peaks were more uncertain and their exact position dependent on the details of the model, such as grid spacing and limits, no satisfactory fit was found without accounting for these small subpopulations. This reflects the limitations in experimental precision and information content of the data.

This aspect is further illustrated in Fig. 2, which shows a series of analyses where only a single kinetic trace obtained at a single concentration was used. As can be expected, the more limited information results in broader distributions. This is true, in particular, for the analysis of the 1 nM trace, which is smooth and does not show characteristic features. (When regularization is switched off, dependent on the discretization of the K_D and k_{off} grid, two or three separate sharp peaks are obtained at different positions, which would represent unreliable and misleadingly detailed information; data not shown.) From the higher concentration trace, however, a reasonably consistent picture of the main peak is obtained. Clearly such an analysis is not the desired configuration, but the ability to estimate binding constants from single kinetic traces can be highly relevant in the practice of using SPR biosensors for studying protein interactions when the surface sites cannot be regenerated. Further, it allows monitoring the initial activity of the immobilized surface sites during the customary stabilization period, and detecting chemical inactivation from successive surface regenerations and other intermittent processes before the surface stabilization (data not shown). The transformation of a single kinetic trace to a K_D-k_{off} distribution with regularization appears superior to a single-site fit, because the width of the distribution will reflect the limited information content of the data used and the associated uncertainty in the obtained binding constants.

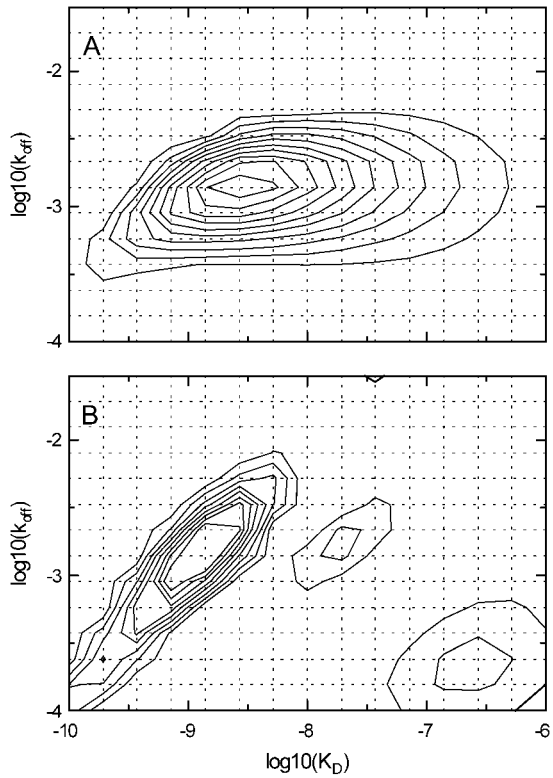

FIGURE 2 Effect of regularization on the estimated distribution of affinity and kinetic rate constants when using only limited information. (*A*) Broad distribution obtained from the analysis of only a single kinetic trace at a low analyte concentration. Analysis is based on the trace obtained at 1 nM shown in Fig. 1 *A*, resulting in an RMS error of 0.25 RU (as compared to 0.35 RU obtained in a single-site fit). (*B*) A more detailed distribution can be estimated on the basis of the kinetic trace 100 nM shown in Fig. 1 *A* (fit with an RMS error 0.24 RU; in comparison, a single site results in a fit with an RMS error of 1.17 RU). The best fit can be achieved by the global analysis at all concentrations as shown in Fig. 1 *E*.

Because the regularization complicates the interpretation of the width of the distribution in Fig. 1 *E* as resulting from micro-heterogeneity of the high-affinity sites, we performed another fit assuming three discrete classes of sites. They were initialized with the average binding parameters taken from the distribution in the main peak, the low-affinity peak, and the trace high-affinity low k_{off} site. Interestingly, the highest affinity site converged at the fringe of the main peak (*triangles* in Fig. 1 *E*) and the quality of the fit was slightly lower (RMS error 0.33 RU) than that of the distribution. This confirms the results from the distribution analysis above and again suggests the presence of micro-heterogeneity of the high-affinity sites.

Next, we examine the potential of accounting for mass transport-limited binding in addition to the binding site distribution. Initially, it is of interest to study simulated data sets of transport-limited binding to single and multiple sites to test what the resolution and limitations of the distribution analysis are. As a test system, we consider two binding sites with $K_{D,1} = 1$ nM and $k_{off,1} = 10^{-3}$/s, and $K_{D,2} = 30$ nM and

$k_{off,2} = 0.015$/s (corresponding to $k_{on,1} = 10^6$/Ms and $k_{on,2} = 5 \times 10^5$/Ms), respectively, with a binding capacity of 100 RU each. The binding was simulated under moderately transport-limited conditions, with a transport rate constant of 10^8 RU/Ms, an order of magnitude to be expected, for example, for molecules of ~10 kDa in a Biacore 3000 flow-cell when using a flow-rate of 1 μl/min. Gaussian noise of 1 RU was added to the theoretical signals calculated at a series of analyte concentrations between 1 and 200 nM (see Fig. 3 *A*). A fit with an impostor transport-limited single site model results in an RMSD of 3.3 RU (with $log_{10}(k_{tr}) = 7.84$ and $K_D = 2.4$ nM, residuals shown Fig. 3 *B*), and a fit permitting a distribution of sites but without transport limitation results in a fit with RMSD = 3.2 (Fig. 3 *C*). Finally, a model for transport-limited binding to a distribution of sites results in an excellent fit with RMSD = 1.07 RU (Fig. 3 *D*) and $log_{10}(k_{tr}) = 7.95$, close to the values underlying the simulation.

As part of the computation process, projections of the error surface are mapped for different values of $log_{10}(k_{tr})$ (at each point calculating the best-fit distribution and ancillary fitting parameters such as baselines and precise injection times). As shown in Fig. 4, it typically exhibits a clear minimum. This shows that the parameter estimate for $log_{10}(k_{tr})$ for transport-influenced systems is well defined by the data.

For comparison, Fig. 5 shows the analysis of simulated data with the same parameters, except for the second site being fivefold lower affinity (5 nM) than the first site (1 nM), in contrast to the data in Fig. 3, which is based on a 30-fold difference. In this case, the best-fit distribution (Fig. 5 *E*) cannot resolve the presence of two sites, and only a single peak is observed with an integrated average K_D of 3.1 nM. Both the distribution of Fig. 5 and that of Fig. 3 exhibit a tail of trace populations toward higher affinity and lower k_{off} sites, which appears to be a result from insufficient information regarding the long-time stability of the complexes from the given data, in combination with the tendency of maximum entropy regularization to produce the broadest peaks consistent with the data. Interestingly, despite the lack of resolution of the two sites in this case, the distribution model still exhibits a distinctly better fit (RMSD = 1.07 RU) than a single-site model (RMSD = 1.39 RU). This improvement of fit with the use of the transport-limited distribution model is a result of the heterogeneity of the sites underlying this simulated data. Therefore, we propose that this improvement can be taken as an indicator of microheterogeneity of the sites.

After examining how the calculated distribution responds to kinetic traces of binding to known sites, we revisited the

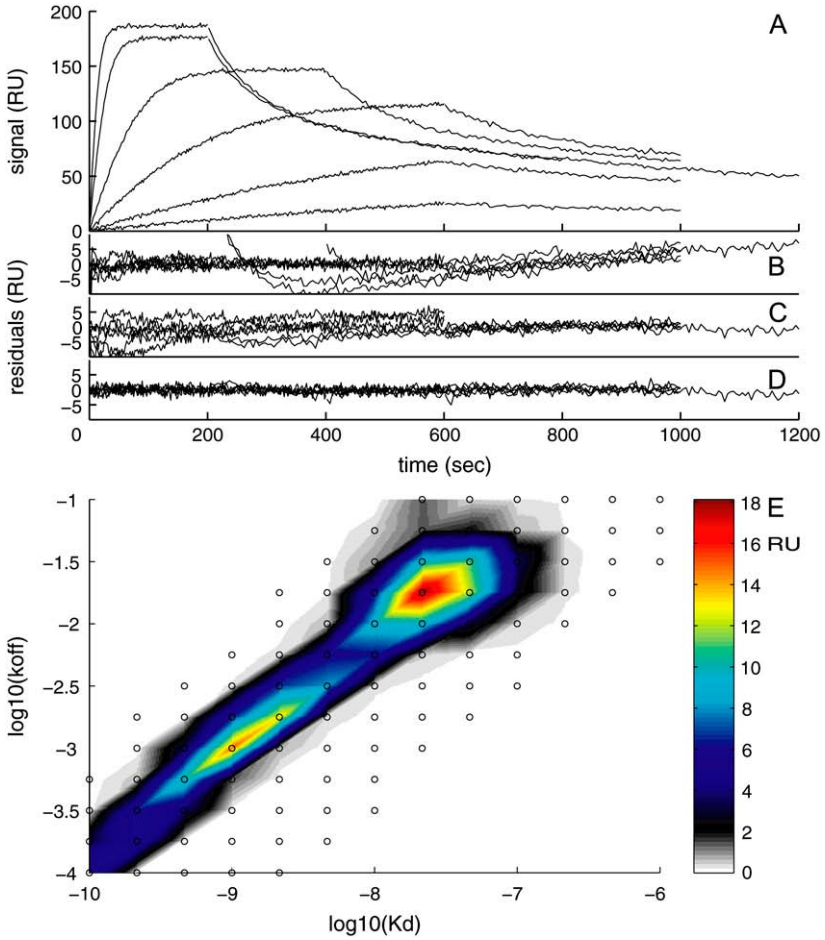

FIGURE 3 Theoretical model system for a transport-limited distribution. (*A*) Binding traces were simulated for analyte concentrations of 1, 3, 10, 30, 100, and 200 nM binding to two sites with $K_{D,1} = 1$ nM and $k_{off,1} = 10^{-3}$/s, and $K_{D,2} = 30$ nM and $k_{off,2} = 0.015$/s, respectively, with a binding capacity of 100 RU each and a transport rate constant of 10^8 RU/Ms. Gaussian noise of 1 RU was added. (*B*) Residuals of a fit with an impostor model of a single, transport-limited site, resulting in $log_{10}(k_{tr}) = 7.84$ and $K_D = 2.4$ nM. (*C*) Residuals of a fit with an impostor distribution model without transport limitation. (*D*) Residuals of a fit with the correct model of a transport-limited distribution, which results in an estimate of $log_{10}(k_{tr}) = 7.95$, and the distribution shown in panel *E*. The grid-points for the numerical computation of the distribution are indicated as small circles. The distribution shown was calculated with maximum entropy regularization scaled to a confidence level of approximately $p = 0.95$.

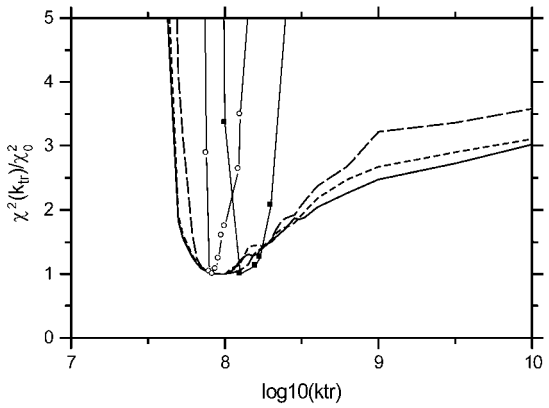

FIGURE 4 Dependence of the quality of fit on the value of the transport rate constant. The value k_{tr} was sequentially fixed to the values indicated, while at each step all other distribution parameters were optimized, including baseline parameters and estimates for the precise injection times. Shown are the resulting best-fit χ^2 values as a function of $log10(k_{tr})$ for the distribution derived from the theoretical model systems in Fig. 3 with (*solid line*) and without (*short dotted line*) considering unknown injection times, respectively, and for the distribution shown in Fig. 5 (*long dashed line*) including the consideration of unknown injection times. Also shown by symbols are the equivalent projections of the error surface from the analysis of the experimental data in Fig. 6 (*open circles*) and Fig. 7 (*solid squares*).

experimental model system from a soluble antigen binding to immobilized antibody used above. For the data shown in Fig. 1, no significant improvement in the quality of fit was achieved by including terms for mass-transport limitation. This is in contrast with the case of immobilization at a higher density, on a CM5 chip with longer carboxymethyl dextran surface, and with binding experiments conducted at a lower flow rate (5 μl/min; Fig. 6). Under these conditions, the binding is transport-influenced, and as a consequence a non-transport-limited distribution model does not fit the data (RMSD = 3.31 RU, Fig. 6 *C*). (Frequently, besides a high RMSD, characteristic diagonally stretched features were observed in the calculated distribution when using an impostor model free of transport-limitation for transport-limited data (not shown)). At the same time, a model for transport-limited binding to a single site also fails to describe the experimental data (RMSD = 3.57 RU, *dotted line* in Fig. 6 *A*, and residuals in Fig. 6 *B*). In contrast, the transport-limited binding to a distribution of surface sites gives an excellent fit with an RMSD of 0.52 RU (Fig. 6 *D*).

Interestingly, the calculated distribution (Fig. 6 *E*) shows a high-affinity site (although at approximately twofold lower affinity as compared to the same interaction observed on the shorter dextran), with a very broad distribution of lower affinity sites (at both lower on-rate and higher off-rate constants). Integration of the distribution indicates that ~28% of total sites belong to this class. They can account, for example, for the characteristic increase in the steady-state region at higher concentrations, as well as (partially) for the multimodal exponential character of the dissociation signal. (These features are highlighted by the difference of the single-site model and the experimental data in Fig. 6 *A*.)

One way of testing the validity of these results is to perform another set of binding experiments with the identical surface, but at different flow rates (Fig. 7). The expectation would be that we observe different transport rate constants, but arrive at very similar distributions. Fig. 7 *C* shows the distribution calculated based on data from the same surface but acquired with a flow-rate of 20 μl/min. As expected, the binding curves shows noticeably faster binding. The same model of transport-limited binding to a distribution of surface sites results again in an excellent fit of the data (with RMSD of 0.52 RU). Again, the distribution is divided into a high-abundance high-affinity site, and a significant population (~23%) of sites with lower affinity and lower on-rate constant. The main peak (with averages of $K_D = 2.3$ nM and $k_{off} = 1.9 \times 10^{-3}$/s) is very similar to the one detected at the lower flow rate ($K_D = 2.6$ nM and $k_{off} = 1.6 \times 10^{-3}$/s). However, there is a clear difference with regard to the details of the distribution of the low affinity sites, with a higher subpopulation of ~100 nM sites in Fig. 7 as compared to Fig. 6. This indicates that the precise characterization of the low-abundance, broadly distributed sites may be beyond the potential of this method.

To maximize the information obtained, we fit globally the binding signals at three flow rates (5, 20, and 40 μl/min) (Fig. 8). Again, the best fit exhibits a main peak at $K_D = 2.5$ nM and $k_{off} = 1.6 \times 10^{-3}$/s, with a global RMSD of 0.61 RU. For practical reasons during the computation we could not optimize data from more than three flow rates at once. However, as a test of the global model, we applied the previously calculated distribution from the 5, 20, and 40 μl/min data as a fixed constraint to a fit of a data set at 1 μl/min, where only the transport rate constant and the effective injection times were treated as floating parameters (Fig. 8 *E*). This resulted in a satisfactory fit with 0.74 RU RMSD. We conclude that the model of transport-limited binding to a distribution of surface sites can provide a rational basis for explaining the experimental data across different flow rates and analyte concentrations close to the experimental noise of data acquisition, and thus take full advantage of the typically very high signal/noise ratio and reproducibility of SPR instruments.

In the global fit, if the sites >16 nM are not allowed, the global RMSD increases from 0.61 to 0.70 RU, and to 0.91 RU when sites >6 nM are excluded, respectively. With these constraints, larger and more systematic residuals at the beginning of the association phase at the higher flow rates were observed, as well as a broad asymmetric main peak tailing toward lower affinity sites comprising 10% of the binding capacity at the highest permitted K_D. Although the decrease in the fit quality is significant (at a total of 14,000 data points), it also illustrates that not very much information on the low-affinity sites is contained in the data, and their details will not be reliable. Nevertheless, the data strongly

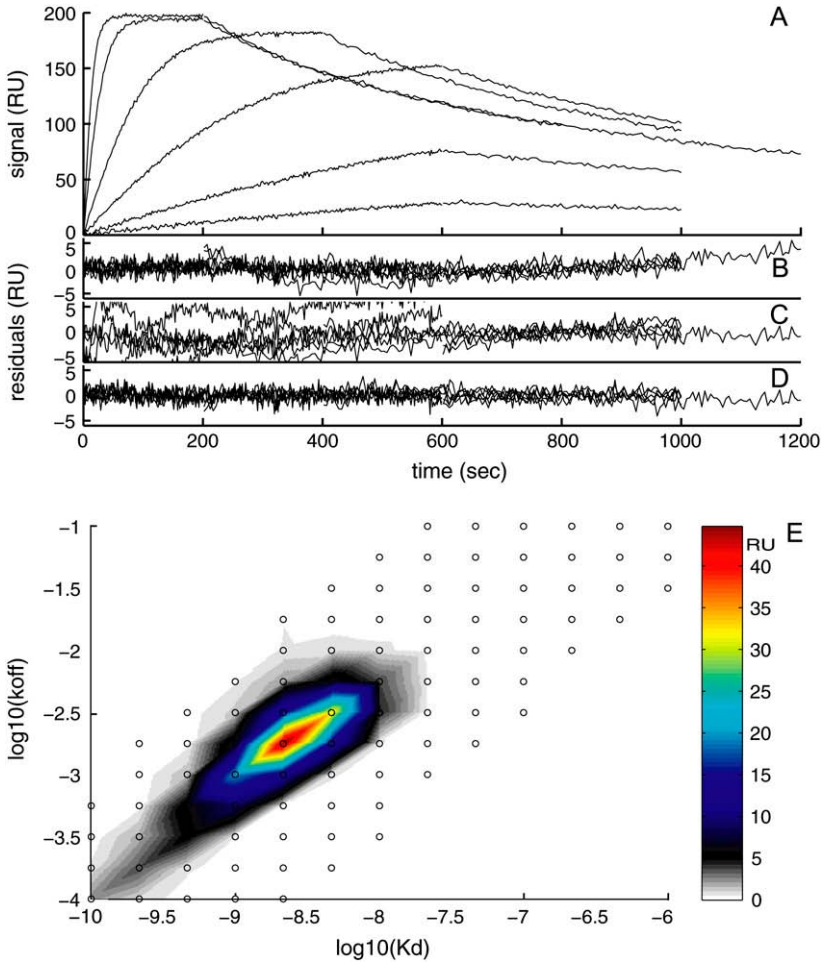

FIGURE 5 Analysis of a theoretical model system for a transport-limited distribution analogous to Fig. 3, but with higher affinity of the second site as compared to Fig. 3 ($K_{D,1} = 1$ nM and $k_{off,1} = 10^{-3}$/s, and $K_{D,2} = 5$ nM and $k_{off,2} = 2.5 \times 10^{-3}$/s, respectively, with a binding capacity of 100 RU each and a transport rate constant of 10^8 RU/Ms), under otherwise identical conditions. (*A*) Binding traces were simulated for analyte concentrations of 1, 3, 10, 30, 100, and 200 nM and Gaussian noise of 1 RU was added. (*B*) Residuals of a fit with an impostor model of a single, transport-limited site, resulting in $log_{10}(k_{tr}) = 8.05$, and $K_D = 2.2$ nM (RMSD 1.39 RU). (*C*) Residuals of a fit with an impostor distribution model without transport limitation. (*D*) Residuals of a fit with the correct model of a transport-limited distribution, which results in an estimate of $log_{10}(k_{tr}) = 7.97$, and the distribution shown in panel *E*. The grid-points for the numerical computation of the distribution are indicated as small circles. The distribution shown was calculated with maximum entropy regularization scaled to a confidence level of approximately $p = 0.95$.

indicate the presence of the low-affinity sites. Higher analyte concentrations should improve this situation, if these sites are of interest. However, in the present context, permitting the degrees of freedom in the fit to describe these low-affinity sites provides an unbiased description of the distribution of high-affinity sites, which can be characterized by integration of the main peak.

The global model results in relatively precise estimates of the transport rate constant, which provides an opportunity to examine the different hypotheses on transport limitation. As indicated by Fig. 4, error estimates of $log10(k_{tr})$ are ~0.1. Fig. 9 shows the best-fit values of k_{tr} as a function of flow rate. The values are based on the global analysis shown in Fig. 8, and are consistent with the flow-rate dependent slope of the initial binding traces depicted in the inset of Fig. 8 *A*. If we assume the flow-rate dependence outlined above (Eq. 6) for surface binding in a laminar flow, the best-fit of the data in Fig. 9 (*dotted line*) leads to an apparent diffusion constant of $D_{app} = 2.7 \times 10^{-7}$ cm^2/s. This value is in contrast to the literature value of 16.5×10^{-7} cm^2/s (taken from (53) and viscosity corrected to 25°C). Further, the measured value seems to correspond to an impossibly high translational frictional coefficient for this molecule, far exceeding even those typical for completely unfolded proteins.

In an attempt to reconcile this discrepancy, we consider an extension of the two-compartment model for transport and binding, where a first, flow-rate dependent step corresponding to Eq. 6 takes place bringing the analyte from the bulk compartment to a compartment adjacent to the surface, followed by a second, flow-rate-independent transport step into a compartment where binding takes place (Eqs. A3–A5). If we assume that the first, flow-rate transport step through the stagnant boundary layer takes place as predicted by Eq. 6 (*solid line* in Fig. 9), a best-fit estimate for the second transport rate constant of 1.6×10^8/s is obtained, with the flow-rate dependence of the total transport shown by the dashed line in Fig. 9. As can be expected, if there is a second rate-limiting but flow-rate-independent transport step, a lower overall flow-rate dependence should be observed. In conclusion, although postulation of an additional transport step can explain the large discrepancy between the expected and measured transport rate constant, the detailed flow-rate dependence is not fully consistent with such a simple model for the second transport step.

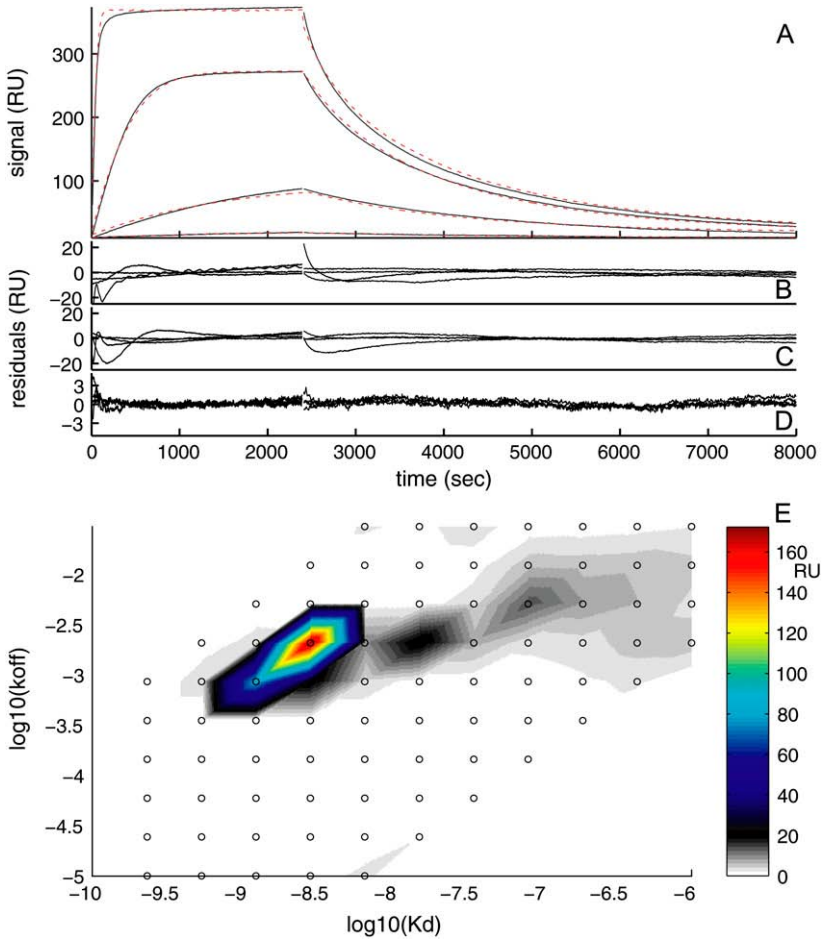

FIGURE 6 Analysis of the transport-influenced binding of soluble β_2-microglobulin to a monoclonal IgG immobilized to longer chain carboxymethylated dextran surface (CM5 chip), at a flow rate of 5 μl/min. (*A*) Experimental data at analyte concentrations of 0.1, 1, 10, and 100 nM (*black solid lines*). Shown as red dotted lines are the best-fit curves based on a model with a single, transport-influenced site. The residuals of this model are shown on an enhanced scale in panel *B*. This single-site model results in an RMSD of the fit of 3.57 RU, an estimate of $log_{10}(k_{tr})$ of 7.98, and estimates for the binding parameters of $K_D = 3.2$ nM and $k_{off} = 1.2 \times 10^{-3}$/s. (*C*) Residuals of a model with a distribution of sites, but in the absence of transport limitation (distribution is not shown). The RMSD with this model is 3.31 RU. (*D*) Residuals from a model for transport-influenced binding to a distribution of sites, with $log_{10}(k_{tr}) = 7.91$, leading to an RMSD of 0.52 RU. (*E*) Calculated distribution with the model for mass transport-influenced binding.

The nature of such a second, rate-limiting transport step is unclear. The immobilization matrix at the sensor surface is made of carboxymethyl dextran. Interestingly, with the data from the ''shorter'' dextran surface at high flow rates, the quality of fit without transport influence is statistically indistinguishable from that with a best-fit transport rate constant in line with the diffusion estimate (Fig. 9, *squares*). (If the data are virtually not or only very little transport-limited, large errors in the estimate of k_{tr} can be expected, since the binding experiment does not depend on k_{tr}.)

To explore the effect of carboxymethyl dextran on the diffusion of β_2-microglobulin, we performed FCS measurements on fluorescently labeled β_2-microglobulin in solutions containing long-chain (500 kDa) carboxymethyl dextran at different concentrations. As visible in Fig. 10, a significant reduction of the translational diffusion coefficient of the protein was observed as the dextran concentration is increased. We believe this is likely caused by hydrodynamic effects. At first glance, the decrease may be attributed to changes in the bulk viscosity of the dextran solution as the Stokes-Einstein relation would suggest. However, this is not necessarily the case for a small probe diffusing in locally inhomogeneous polymeric solution, contrary to assumptions on which the Stokes-Einstein relation is based. In this case, one needs to consider a local microviscosity of the dextran solution experienced by the probe (54,55). However, only 29% decrease was observed at the highest concentration tested (23.7 mg/ml, which is in the approximate range of the concentration estimated in the immobilization matrix (18), a number that will be dependent, for example, on assumptions of matrix thickness). This effect was found to be far smaller than required to explain the rate-limiting transport step.

Because the compartment model is the simplest possible formal approach to account for a transport step, we believe it can serve as a first-order approximation for the mass transport effects on binding kinetics. If the binding kinetics is only slightly affected by mass transport, irrespective of the precise physical nature of the transport step. However, at stronger mass transport limitation, when it becomes rate-limiting, what is considered the physical basis for the compartments is actually not well mixed. In fact, a hallmark of reaction-diffusion problems are spatial inhomogeneities (56), and that moving reaction fronts can be established. In this case, the details of spatial flow of analyte and the spatial distribution of surface sites typically become crucial. In the evanescent field biosensor, the detection is spatially

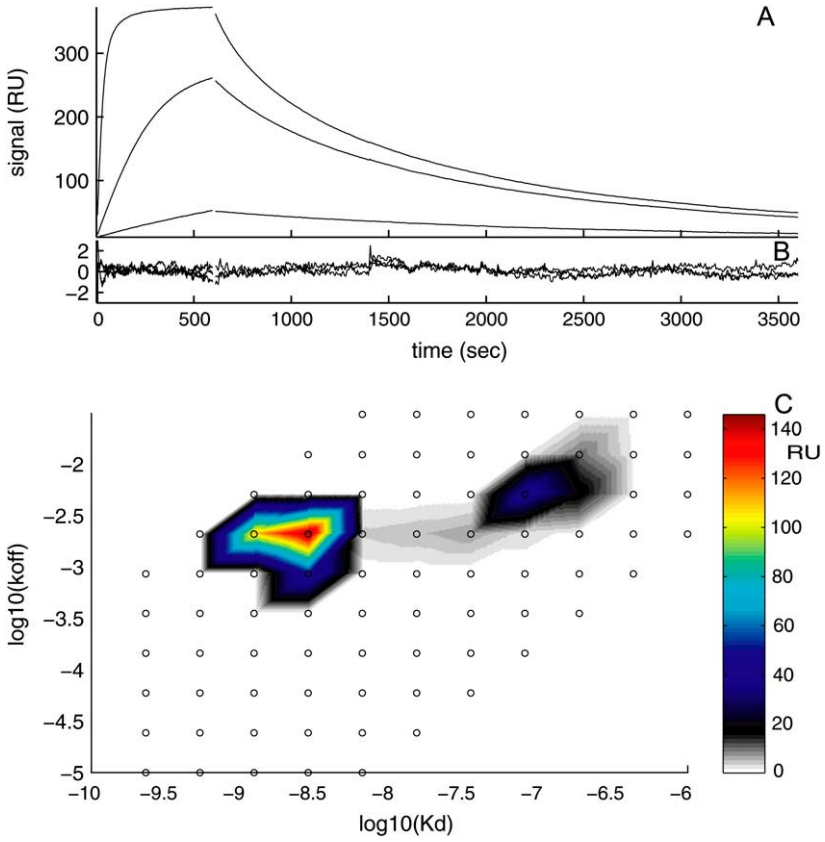

FIGURE 7 Analysis of the transport-influenced binding to the same surface as shown in Fig. 6, but at a higher flow-rate of 20 μl/min. (*A*) Experimental data at analyte concentrations of 1, 10, and 100 nM (*black solid lines*). (*B*) Residuals from a model for transport-influenced binding to a distribution of sites, with $log_{10}(k_{tr}) = 8.09$, leading to an RMSD of 0.52 RU. (*C*) Calculated distribution.

inhomogeneous: it is laterally confined to a sensing area, where the sensitivity exponentially decays with increasing distance from the surface. The combination of spatially inhomogeneous transport-limited binding with spatially inhomogeneous detection can give rise to characteristic signals (26): in the association phase—instead of the linear increase preceding saturation, an increasing slope can signify the time when the reaction front reaches a more sensitive detection volume; at the start of the dissociation phase—if the analyte supply is stopped with the reaction front located at a significant sensitivity gradient, local diffusion can transport analyte into the more sensitive regions, which produces a signal increase that can more than compensate the signal loss from analyte dissociation and transport out of the sensing volume. These effects were predicted computationally from a transport model for binding within the immobilization matrix (26).

To verify experimentally the existence of such gradients and their characteristic signals, we conducted experiments under virtually complete mass transport control. This was achieved by immobilization of a monoclonal antibody HyHEL-10 at high surface density (Fig. 11). From the binding traces of the soluble antigen, the sigmoid-shaped association phase can be discerned. Also, when the association phase was stopped at the signal level where positive curvature was observed, the following dissociation reproducibly showed a small, but significant increase in the dissociation signal. There is no evidence that this was caused by baseline drifts, which are typically much smaller in magnitude. Similar traces with these characteristic qualitative features from spatial gradients were observed with other systems (data not shown). This exhibits the limits of the compartment model. Therefore, detailed modeling was not pursued.

DISCUSSION

In this article, we report a new approach to account for mass transport influence on the binding kinetics of soluble analyte molecules to surface-immobilized sites, which accounts for potential heterogeneity of the surface sites without a priori assumptions on their number or kinetic rate constants. This is an extension of the previously introduced approach for the analysis of distributions of affinity and rate constants of surface sites from experimental kinetic surface binding traces (22). The inclusion of a mass transport step changes the nature of the mathematical model from a superposition of multiple independent binding events to a nonlinear, coupled system of binding reactions that are mutually linked through the competition for limited analyte close to the surface. This problem requires different computational tools, which were implemented in a computer program that permits modeling of experimental data. This approach permits simultaneous consideration of the two most commonly encountered hurdles for using optical biosensors analytically to discern

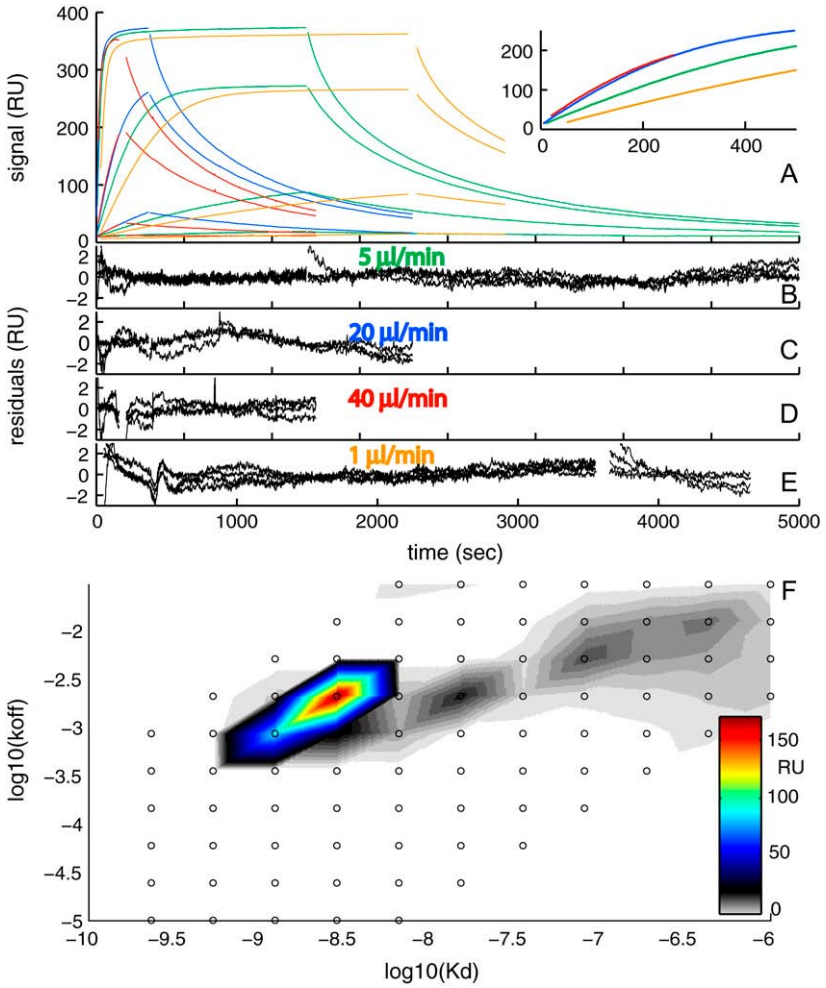

FIGURE 8 Global fit of the surface binding data acquired at 5, 20, and 40 μl/min with a model for transport-influenced binding to a distribution of surface sites. The transport rate constant and effective injection start times are treated as unknowns local to each data set at the different flow rates (see Fig. 9). The distribution from the 5 μl/min data was taken as starting guess in the distribution to be optimized, and no regularization was used. (*A*) Experimental data at 1 (*orange*), 5 (*green*), 20 (*blue*), and 40 (*red*) μl/min for analyte concentrations of 0.1, 1, 10, and 100 nM (no 0.1 nM data available at 20 μl/min). The inset expands the initial association data at an analyte concentration of 10 nM for all flow rates. The results of the global fit are at 5 μl/min: $log_{10}(k_{tr}) = 7.91$ with an RMSD of 0.53 RU (*B*), at 20 μl/min: $log_{10}(k_{tr}) = 8.18$ with an RMSD of 0.79 RU (*C*), at 40 μl/min: $log_{10}(k_{tr}) = 8.21$ with an RMSD of 0.66 RU (*D*). (*E*) Given the distribution from the fit of the three high flow rates, we applied the distribution as a constant prior knowledge to the data at 1 μl/min, here optimizing solely the transport rate constant, resulting in $log_{10}(k_{tr}) = 7.62$ with an RMSD of 0.74 RU. (*F*) Best-fit distribution, calculated without maximum entropy regularization.

the thermodynamic and kinetic characteristics of protein interactions. It is restricted to reactions that proceed individually as simple association and dissociation steps, without kinetically limiting conformational changes, or cooperative site-site interactions. However, in the absence of evidence to the contrary when working with specific systems, for many cases this seems reasonable and is the most parsimonious assumption.

As a result of the analysis, estimates are obtained for the distribution of kinetic and affinity constants of the surface sites, as well as a transport rate constant. Further, typically a fit of the data is obtained close to the experimental noise of the data acquisition, thus taking full advantage of the typically extremely high signal/noise ratio and reproducibility of the time-course of surface binding recorded with evanescent wave biosensors, such as, for example, surface plasmon resonance biosensors. This is in contrast to most of the discrete binding models considered here (Figs. 1 *B* and 6 *B*) and found in the literature, which frequently exhibit systematic deviations in the residuals, a result that in other disciplines would be taken as an indication to reject the model. The finding that it is possible to obtain consistent fits with residuals close to the noise of data acquisition suggests that the same stringent criteria can be applied when modeling SPR surface binding data.

With the goal to characterize the intrinsic binding properties of the interacting proteins under study, it is straightforward to integrate the main peak of the distribution, and calculate average affinity and rate constants. The current approach will take into account all available data and transforms them into a space of binding constants, where a distinction between sites of interest or nonspecific sites can be made. Beyond the examples shown in this article, other earlier applications of this approach can be found, for example, in the characterization of antibody-antigen interactions (17,57,58), whereas the multimodal character of the distribution was of additional interest in studies of the interaction of integrin domains with fibrinogen (59).

Regularization is applied to suppress detail in the calculated distributions beyond the level statistically warranted by the experimental data, a common strategy for solving Fredholm integral equations (28–30,50). To highlight the

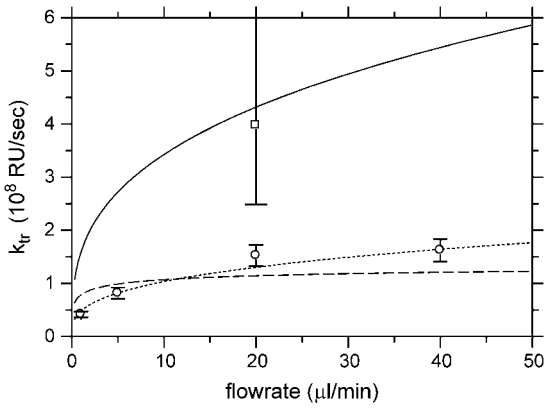

FIGURE 9 Analysis of the dependence of the transport rate constant on the flow rates. Circles depict the estimates of the transport rate constant on the ''long dextran'' (CM5) surface from the global analysis of Fig. 8, with error bars corresponding to an error in $log_{10}(k_{tr})$ of 0.1. The square is the corresponding value obtained for the ''short'' dextran (F1) surface of Fig. 1. The dotted line is the best-fit from the compartment model for the transport through the stagnant boundary layer according to Eq. 6. It results in an apparent diffusion coefficient of 2.7×10^{-7}cm^2/s. Using the known bulk diffusion coefficient of β_2-microglobulin (16.5×10^{-7}cm^2/s, from (53) and viscosity corrected to 25°C), the flow rate dependence of the transport rate constants indicated by the solid black line is expected. If a three-compartment model is used that combines the expected flow-dependent transport through the stagnant boundary with a second, flow-rate independent transport step, a best-fit value of the second transport rate constant of 1.6×10^8 RU/s is obtained. In this case, the total flow-rate dependence of the combined transport is shown by the dashed solid line.

property of the regularization, we have shown that single traces can be subjected to data analysis. In this case, the regularization results in a broad distribution, which reflects the limited information that is contained in surface binding at a single analyte concentration. We believe that this point is a useful feature that permits conservative interpretation. In

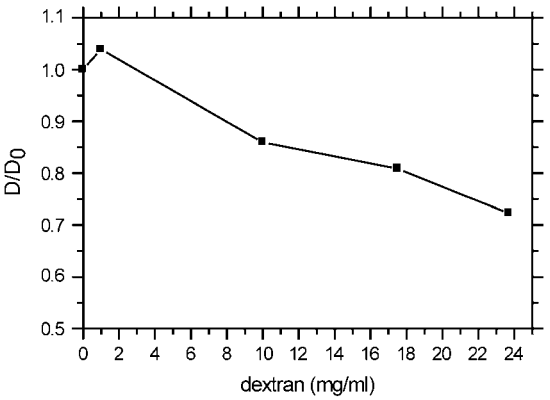

FIGURE 10 Relative decrease of the diffusion coefficient of β_2-microglobulin dependent on the concentration of carboxymethyl dextran in the sample. Data were determined from FCS measurements. The coefficients were scaled with D_o, the coefficient of β_2-microglobulin in the buffer only (no dextran).

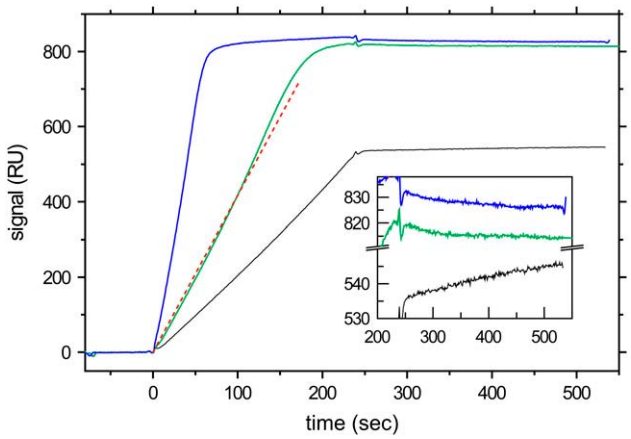

FIGURE 11 Binding signal under virtually complete mass transport control. HyHel-10 mAb immobilized to a long-chain carboxymethyl dextran matrix (CM5 chip), and binding of 10 nM (*black*), 20 nM (*green*), and 60 nM (*blue*) soluble antigen (hen egg lysozyme) at a flow rate of 5 μl/min. To highlight the sigmoid-shaped binding curve with increasing slope, a straight (*red dotted line*) line is plotted for comparison. The inset shows the dissociation trace after incomplete association at 10 nM in enlarged scale. The increasing signal is significant and highly reproducible.

practice, such analyses of single traces can be of importance when no method for reversible regeneration of the surface sites can be found, or when assessing possible irreversible effects of chemical regeneration on the affinity distribution. Even with ''complete'' sets of surface binding traces at different concentrations, with typical signal/noise ratio of commercial SPR sensors, our simulations indicate that two sites with a fivefold difference in affinity may not be resolved, unless experiments were conducted with higher immobilization level. (In contrast, a fivefold shift in the affinity of a single site can be clearly detected.) However, even in this case, the presence of micro-heterogeneity in the affinity can be qualitatively deduced (and distinguished from the finite width produced by regularization from noisy data of a true single site) from the comparison of the fit with a distribution model to a fit with a traditional discrete single-site model. Such evidence for the presence of microheterogeneity was reported for immobilized monoclonal antibodies interacting with soluble antigen (17). We believe that the heterogeneity may be introduced by structurally heterogeneous attachment and/or by the heterogeneity in the physical microenvironment in different regions of the immobilization matrix.

In contrast to the main peak corresponding to high-affinity sites, we also detected a range of lower affinity sites in the analysis of our experimental systems. In Figs. 6 and 7, these low affinity sites contribute 20–30% of the total surface sites, and the quality of fit decreases significantly when they are excluded. Unfortunately, their precise distribution could not be reliably determined. It may be possible to better characterize such low-affinity sites by applying higher analyte concentrations. There are many possible reasons that

may produce low-affinity sites, ranging from locally more unfavorable physical microenvironment, steric constraints for analyte binding by the dextran matrix or immobilized protein in the close vicinity of the binding epitope, to the chemical immobilization locking some protein population into an unfavorable conformation. Signals from the adsorption of analyte to the sensor surface should be eliminated, to a large degree, by use of a reference surface and signal subtraction, although the reference surface and the active surface are not completely identical (42). In any case, even where the goal of the analysis is the determination of the average affinity of the main, high-affinity population, it is important to account for the low-affinity sites (even if they are not well characterized), so that their presence does not introduce bias in the analysis of the high-affinity sites. Further, if the low-affinity side-reactions are not a contaminant, but of intrinsic interest, for example, when studying nonspecific adsorption properties of surfaces, the present approach can allow one to discriminate and quantify these sites.

For transport-influenced surface binding, the approach described here provides an estimate for the transport rate constant. This is an opportunity to study the transport process. As shown in Fig. 4, the transport rate constants can be well determined by the data analysis, and are not much correlated with the binding parameters of the distribution. It has been proposed that the transport rate constants can be determined by globally fitting binding data from surfaces with different surface densities of sites (e.g., in (25)). However, based on the observation above from experiments that immobilization produces populations of different affinity, it is not obvious that different surfaces with different total surface concentration produce the same affinity distribution. Further study is needed to find out the extent to which surface site distribution changes with different immobilization levels. To avoid this potential problem, in the present work we have determined the transport rate constants by globally fitting data collected from the same surface, at different analyte flow rates, which ensures the distribution to be unchanged.

Transport through the stagnant boundary layer of a laminar flow is well understood (33). Myszka et al. (25) have proposed that the resulting transport rate constants can be used to estimate a diffusion coefficient, based on approximations for transport in a laminar flow. However, when applied to the data derived from the long-chain CM dextran, in the present case, the apparent diffusion coefficient was sixfold smaller than expected, and had a lower than expected flow-rate dependence. This highlights that transport-limiting steps other than stagnant boundary layer of the laminar flow can be present.

The origin of this additional transport step is unknown. However, the experimental binding traces were well described by a model without transport limitation when working with the ''short'' chain CM dextran matrix (F1 chip), while they were significantly transport-influenced on the ''long'' chain CM dextran matrix (CM5 chip) (at the same flow rate). Based on theoretical considerations, we have proposed previously that transport within the dextran matrix can be rate-limiting for systems with hindered diffusion and poor partitioning into the matrix (26). Other groups have described theoretical models considering binding within the thickness of the dextran matrix (4,60). Based on an effective rate constants approach, Wofsy and Goldstein have questioned which, if any, Biacore experiments could potentially exhibit transport limitation arising from the thickness of the matrix (37). In addition to the experiments in this study using a readily available antibody-antigen system, effects of the dextran matrix on mass transport in surface binding were experimentally observed previously for some systems (61–63), while no effects were found in others (64,65). This suggests that whether or not the thickness of the carboxymethyl dextran is contributing to the transport limitation may depend strongly on the properties of the proteins considered, but may not be uncommon. As a consequence, for theoretical models the question arises which mechanism might be responsible for these effects, and the difficulty of estimating realistic parameter values. Further, in principle, matrix-related influences on analyte transport properties not directly related to its finite thickness cannot be excluded.

Effects that we proposed earlier to likely contribute to lowering the mass transport in the dextran matrix are 1), the size-dependent partitioning (26,66); 2), hindered diffusion of proteins through polymer matrix with immobilized macromolecules (26,67,68); and 3), nonspecific interactions with the sensor surface (20). Based on estimates for the partition coefficient as described in Schuck (26) and on the measured diffusion of β_2-microglobulin in CM dextran solution, the first two effects would only amount to a total reduction by a factor two. The third factor is very difficult to assess by SPR, but could potentially contribute more significantly, if rapidly reversible nonspecific sites create a nondiffusing fraction of analyte, thus reducing the effective diffusion coefficient (20,69). A simple estimation shows that within the uncertainty of the biosensor signal this effect could amount to one or two orders of magnitude (20), and it might explain the variability in the results of studies on the influence of the CM dextran with different systems. However, such effects should also have been observed in the FCS experiments, unless there were differences in the CM dextran used in our solution experiments to the one attached to the CM5 chip, or fundamental differences in the interaction of analyte with free CM dextran versus an immobilized and functionalized CM dextran brush. The latter does not appear unlikely, considering steric constraints and the nonuniform density distribution of attached polymers (70), possibly altered hydrodynamic interactions in the vicinity of a surface (71), conformational changes of the dextran introduced by electrostatic interactions of the carboxymethyl groups (including sensitivity to pH and possible partial collapse at high

ionic strength) (72), the local charge density and local pH influencing the interaction with the protein (73), and the possibility of the covalent immobilization of protein changing the structure (61,74) and/or crosslinking the CM dextran.

A qualitative prediction from our previous theoretical model of transport through the dextran matrix perpendicular to the sensor surface was that under conditions of strong transport limitation, gradients in sensitivity combined with moving gradients of binding should generate characteristic signal artifacts of concave association curves, and under some circumstances a paradoxically rising signal is concurrent with the dissociation of analyte from the surface. Using a high-affinity antibody with well-understood binding kinetics and thermodynamics (43), when experimental conditions of transport-limited binding were applied, these predicted sensor-related artifacts were reproducibly observed. While this demonstrates experimentally the presence of gradients within the sensing volume, it does not allow distinguishing gradients parallel and perpendicular to the sensor surface. Zacher and Wischerhoff have examined the time-course of binding into a dextran matrix by simultaneous two-color SPR, and observed the binding time-course that proceeded from the outer to the inner regions of the matrix during the immobilization of streptavidin, followed by selective binding to the outer regions of the dextran layer for biotinylated protein A (74). This experimental evidence for spatial gradients supports the notion that conditions can exist in practice for which the diffusion perpendicular to the sensor surface is strongly limited.

Although the general practice of low immobilization levels and high flow rates should minimize transport influence in the surface binding kinetics, it does not guarantee that one can observe solely the chemical reaction kinetics. The data presented here and the data reported in the literature present a more complicated picture of binding to protein sites immobilized in CM dextran at surfaces. For this reason, we believe that the analytical approach proposed here for considering both transport influence as well as an ensemble of surface sites with heterogeneous binding properties, without the ad hoc assumption of discrete sites, and without prior assumptions on the nature of the transport step, will be useful. However, the analysis of the surface binding kinetics should be restricted to the case of moderate transport influence, where we believe the compartment model approximation holds irrespective of the physical details of the spatial mass transport, and where the experimental data still carry information on the intrinsic molecular binding kinetics of interest. We found that consideration of surface heterogeneity generally allows a greatly improved fit of the data, with residuals typically close to the noise of data acquisition, suggesting that microheterogeneity of immobilized proteins on the sensor surface may be significant. This method provides a rational criterion to distinguish sites of interest from contaminating side reactions. It may also be useful both to study surface immobilization and protein adsorption to surfaces.

APPENDIX

Effective rate constants approximation for transport-limited binding to a distribution of surface sites

First, we consider a two-compartment model for transport with rate constant k_{tr} from a bulk compartment at c_0 to a surface compartment at c_s, followed by reversible binding to a single class of surface sites. As outlined in Methods above, the rate constants for the signal s and surface concentration c_s are

$$\begin{aligned}\frac{ds}{dt} &= k_{on}c_s(s_{max} - s) - k_{off}s\\ \frac{dc_s}{dt} &= k_{tr}(c_0 - c_s) - \frac{ds}{dt}.\end{aligned} \tag{A1}$$

As is well known, the assumption of steady-state conditions, where $ds/dt \gg dc_s/dt$, leads to the approximation of the binding progress by effective rate constants k^* with

$$\begin{aligned}\frac{ds}{dt} &= k^*_{on}c_0(s_{max} - s) - k^*_{off}s\\ \frac{k^*_{on}}{k_{on}} &= \frac{k^*_{off}}{k_{off}} = \frac{1}{1 + k_{on}(s_{max} - s(t))/k_{tr}},\end{aligned} \tag{A2}$$

where the reduction of binding rate constants is dependent on the amount of free surface sites s_{max}–$s(t)$, i.e., the relative probability of binding versus transport. For strongly transport-limited binding, the ratio $k_{on}s_{max}/k_{tr} \gg 1$, while for moderately transport-influenced binding, $k_{on}s_{max}/k_{tr} < 1$.

To examine the flow rate-dependence of our experimentally determined transport rate constant, we consider a hypothetical three-compartment model, where a first, flow-rate dependent transport step with $k_{tr,1}(\nu)$ from a well-mixed bulk compartment at concentration c_0 to a stagnant boundary layer compartment (also internally well mixed) at concentration c_s is followed by a second, flow-rate independent step with $k_{tr,2}$ to a second compartment in the sensor matrix (likewise internally well mixed) with concentration c_m:

$$\begin{aligned}\frac{ds}{dt} &= k_{on}c_m(s_{max} - s) - k_{off}s\\ \frac{dc_m}{dt} &= k_{tr,2}(c_s - c_m) - \frac{ds}{dt}\\ \frac{dc_s}{dt} &= k_{tr,1}(\nu)(c_0 - c_s) - k_{tr,2}(c_s - c_m).\end{aligned} \tag{A3}$$

Similar to the two-compartment model above, it is possible to determine effective rate constants under steady-state conditions ($dc_s/dt \approx 0$ and $dc_m/dt \approx 0$). Under this condition, it can be shown that transport can be described by an effective overall transport rate constant, which is the harmonic mean of the two rate constants

$$k^{-1}_{tr,all} = k_{tr,1}(\nu)^{-1} + k^{-1}_{tr,2} \tag{A4}$$

(i.e., the characteristic transport times are additive), for which the usual relationships for the reduced apparent rate constants hold:

$$\frac{ds}{dt} = k^*_{on} c_0 (s_{max} - s) - k^*_{off} s$$
$$\frac{k^*_{on}}{k_{on}} = \frac{k^*_{off}}{k_{off}} = \frac{1}{1 + k_{on}(s_{max} - s(t))/k_{tr,all}}. \quad \text{(A5)}$$

Again, the effective rate constants depend only on the relative probability of binding versus combined transport.

These compartment models can be extended to the binding to many independent binding sites i with maximal binding capacity $s_{max,i}$. The rate constants were described above (Eqs. 7 and 8) and solved to obtain the time-course of binding to each site. In the picture of effective rate constants, we can combine Eqs. 7 and 8 and arrive at an expression for the overall binding,

$$\sum_i \frac{ds_i}{dt} = \sum_i k^*_{on,i} c_0 (s_{max,i} - s_i) - \sum_i k^*_{off,i} s_i$$
$$\frac{k^*_{on,i}}{k_{on,i}} = \frac{k^*_{off,i}}{k_{off,i}} = \frac{1}{1 + \sum_j k_{on,j}(s_{max,j} - s_j(t))/k_{tr}}, \quad \text{(A6)}$$

where each effective rate constant is reduced by the same factor that depends on the total probability of binding versus transport.

For the three-compartment model, analogously one can obtain the relationship

$$\sum_i \frac{ds_i}{dt} = \sum_i k^*_{on,i} c_0 (s_{max,i} - s_i) - \sum_i k^*_{off,i} s_i$$
$$\frac{k^*_{on,i}}{k_{on,i}} = \frac{k^*_{off,i}}{k_{off,i}} = \frac{1}{1 + \sum_j k_{on,j}(s_{max,j} - s_j(t))/k_{tr,all}}, \quad \text{(A7)}$$

with the effective total transport rate constant as described in Eq. A4. As a consequence, for transport-limited surface binding with multistep transport, what can be determined from the surface binding data is only the overall transport rate constant.

This work was supported in part by the Intramural Research Program of the National Institutes of Health. R.C.W. acknowledges support from the National Science Foundation and the Welch Foundation (grant No. E-1264).

REFERENCES

1. Vijayendran, R. A., and D. E. Leckband. 2001. A quantitative assessment of heterogeneity for surface-immobilized proteins. *Anal. Chem.* 73:471–480.
2. Sips, R. 1948. On the structure of a catalyst surface. *J. Chem. Phys.* 16:490–495.
3. Koopal, L. K., and C. H. W. Vos. 1993. Adsorption on heterogeneous surfaces. Calculation of the adsorption energy distribution function or the affinity spectrum. *Langmuir*. 9:2593–2605.
4. Lebedev, K., S. Mafe, and P. Stroeve. 2006. Convection, diffusion and reaction in a surface-based biosensor: modeling of cooperativity and binding site competition on the surface and in the hydrogel. *J. Colloid Interface Sci.* 296:527–537.
5. Nisonoff, A., and D. Pressman. 1958. Heterogeneity and average combining constants of antibodies from individual rabbits. *J. Immunol.* 80:417–428.
6. Steckbeck, J. D., H. J. Grieser, T. Sturgeon, R. Taber, A. Chow, J. Bruno, M. Murphy-Corb, R. C. Montelaro, and K. S. Cole. 2006. Dynamic evolution of antibody populations in a rhesus macaque infected with attenuated simian immunodeficiency virus identified by surface plasmon resonance. *J. Med. Primatol.* 35: 248–260.
7. Yeung, C., and D. E. Leckband. 1997. Molecular level characterization of microenvironmental influences on the properties of immobilized proteins. *Langmuir*. 13:6746–6754.
8. Rabbany, S. Y., R. Piervincenzi, L. Judd, A. W. Kusterbeck, R. Bredehorst, K. Hakansson, and F. S. Ligler. 1997. Assessment of heterogeneity in antibody-antigen displacement reactions. *Anal. Chem.* 69:175–182.
9. Kloss, A. A., N. Lavrik, C. Yeung, and D. E. Leckband. 2000. Effect of the microenvironment on the recognition of immobilized cytochromes by soluble redox proteins. *Langmuir*. 16:3414–3421.
10. Wilson, D. S., and S. Nock. 2002. Functional protein microarrays. *Curr. Opin. Chem. Biol.* 6:81–85.
11. Taitt, C. R., G. P. Anderson, and F. S. Ligler. 2005. Evanescent wave fluorescence biosensors. *Biosens. Bioelectron.* 20:2470–2487.
12. O'Shannessy, D. J. 1994. Determination of kinetic rate and equilibrium binding constants for macromolecular interactions: a critique of the surface plasmon resonance literature. *Curr. Opin. Biotechnol.* 5:65–71.
13. O'Shannessy, D. J., and D. J. Winzor. 1996. Interpretation of deviations from pseudo-first-order kinetic behavior in the characterization of ligand binding by biosensor technology. *Anal. Biochem.* 236: 275–283.
14. Schuck, P. 1997. Use of surface plasmon resonance to probe the equilibrium and dynamic aspects of interactions between biological macromolecules. *Annu. Rev. Biophys. Biomol. Struct.* 26:541–566.
15. Cooper, M. A. 2002. Optical biosensors in drug discovery. *Nat. Rev. Drug Discov.* 1:515–528.
16. Livache, T., E. Maillart, N. Lassalle, P. Mailley, B. Corso, P. Guedon, A. Roget, and Y. Levy. 2003. Polypyrrole based DNA hybridization assays: study of label free detection processes versus fluorescence on microchips. *J. Pharm. Biomed. Anal.* 32:687–696.
17. Sundberg, E. J., P. S. Andersen, I. I. Gorshkova, and P. Schuck. Surface plasmon resonance biosensing in the study of ternary systems of interacting proteins. *In* Protein Interactions: Biophysical Methods for Complex Systems. P. Schuck, editor. Springer, New York. In press.
18. Karlsson, R., H. Roos, L. Fägerstam, B. Persson. 1994. Kinetic and concentration analysis using BIA technology. *Meth. Companion Meth. Enzymol.* 6:99–110.
19. Glaser, R. W., and G. Hausdorf. 1996. Binding kinetics of an antibody against HIV p24 core protein measured with real-time biomolecular interaction analysis suggest a slow conformational change in antigen p24. *J. Immunol. Methods*. 189:1–14.
20. Schuck, P. 1997. Reliable determination of binding affinity and kinetics using surface plasmon resonance biosensors. *Curr. Opin. Biotechnol.* 8:498–502.
21. Schuck, P., D. B. Millar, and A. A. Kortt. 1998. Determination of binding constants by equilibrium titration with circulating sample in a surface plasmon resonance biosensor. *Anal. Biochem.* 265:79–91.
22. Svitel, J., A. Balbo, R. A. Mariuzza, N. R. Gonzales, and P. Schuck. 2003. Combined affinity and rate constant distributions of analyte or ligand populations from experimental surface binding and kinetics and equilibria. *Biophys. J.* 84:4062–4077.
23. Glaser, R. W. 1993. Antigen-antibody binding and mass transport by convection and diffusion to a surface: a two-dimensional computer model of binding and dissociation kinetics. *Anal. Biochem.* 213:152–161.
24. Balgi, G., D. E. Leckband, and J. M. Nitsche. 1995. Transport effects on the kinetics of protein-surface binding. *Biophys. J.* 68:2251–2260.
25. Myszka, D. G., X. He, M. Dembo, T. A. Morton, and B. Goldstein. 1998. Extending the range of rate constants available from BIACORE: interpreting mass transport-influenced binding data. *Biophys. J.* 75:583–594.
26. Schuck, P. 1996. Kinetics of ligand binding to receptor immobilized in a polymer matrix, as detected with an evanescent wave biosensor. I. A

computer simulation of the influence of mass transport. *Biophys. J.* 70:1230–1249.

27. Phillips, D. L. 1962. A technique for the numerical solution of certain integral equations of the first kind. *J. Assoc. Comput. Mach.* 9: 84–97.
28. Provencher, S. W. 1982. A constrained regularization method for inverting data represented by linear algebraic or integral equations. *Comput. Phys. Comm.* 27:213–227.
29. Puziy, A. M. 1999. Use of CONTIN for calculation of adsorption energy distributions. *Langmuir.* 15:6016–6025.
30. Haber-Pohlmeier, S., and A. Pohlmeier. 1997. Kinetics and equilibrium of the ion exchange of Cd^{2+} at Na-montmorillonite: analysis of heterogeneity by means of the regularization technique CONTIN. *J. Colloid Interface Sci.* 188:377–386.
31. Ober, R. J., and E. S. Ward. 2002. Compensation for loss of ligand activity in surface plasmon resonance experiments. *Anal. Biochem.* 306: 228–236.
32. Schuck, P., and A. P. Minton. 1996. Analysis of mass transport limited binding kinetics in evanescent wave biosensors. *Anal. Biochem.* 240: 262–272.
33. Lok, B. K., Y.-L. Cheng, and C. R. Robertson. 1983. Protein adsorption on crosslinked polydimethylsiloxane using total internal reflection fluorescence. *J. Colloids Interface Sci.* 91:104–116.
34. Stenberg, E., B. Persson, H. Roos, and C. Urbaniczky. 1991. Quantitative determination of surface concentration of protein with surface plasmon resonance using radiolabeled proteins. *J. Colloids Interface Sci.* 143:513–526.
35. Press, W. H., S. A. Teukolsky, W. T. Vetterling, and B. P. Flannery. 1992. Numerical Recipes in C. University Press, Cambridge, UK.
36. Ruhe, A., and P. Å. Wedin. 1980. Algorithms for separable nonlinear least squares problems. *SIAM Rev.* 22:318–337.
37. Wofsy, C., and B. Goldstein. 2002. Effective rate models for receptors distributed in a layer above a surface: application to cells and Biacore. *Biophys. J.* 82:1743–1755.
38. Biacore. 2003. Biacore 3000 Instrument Handbook, Uppsala, Sweden.
39. Ferracci, G., R. Miquelis, S. Kozaki, M. Seagar, and C. Leveque. 2005. Synaptic vesicle chips to assay botulinum neurotoxins. *Biochem. J.* 391:659–666.
40. Schuck, P., L. F. Boyd, and P. S. Andersen. 1999. Measuring protein interactions by optical biosensors. *In* Current Protocols in Protein Science. J. E. Coligan, B. M. Dunn, H. L. Ploegh, D. W. Speicher, and P. T. Wingfield, editors. John Wiley & Sons, New York.
41. O'Shannessy, D. J., M. Brigham-Burke, and K. Peck. 1992. Immobilization chemistries suitable for use in the BIAcore surface plasmon resonance detector. *Anal. Biochem.* 205:132–136.
42. Ober, R. J., and E. S. Ward. 1999. The choice of reference cell in the analysis of kinetic data using BIACORE. *Anal. Biochem.* 271: 70–80.
43. Xavier, K. A., and R. C. Willson. 1998. Association and dissociation kinetics of anti-hen egg lysozyme monoclonal antibodies HyHEL-5 and HyHEL-10. *Biophys. J.* 74:2036–2045.
44. Chen, Y., J. D. Muller, K. M. Berland, and E. Gratton. 1999. Fluorescence fluctuation spectroscopy. *Methods.* 19:234–252.
45. Webb, W. W. 2001. Fluorescence correlation spectroscopy: Inception, biophysical experimentations, and prospectus. *Appl. Opt.* 40:3969–3983.
46. Rigler, R., and E. S. Elson. 2001. Fluorescence Correlation Spectroscopy: Theory and Applications. Springer, New York.
47. Aragon, S. R., and R. Pecora. 1976. Fluorescence Correlation Spectroscopy. *J. Chem. Phys.* 64:1792–1803.
48. Michelman-Ribeiro, A., H. Boukari, R. Nossal, and F. Horkay. 2004. Structural changes in polymer gels probed by fluorescence correlation spectroscopy. *Macromolecules.* 37:10212–10214.
49. Boukari, H., R. Nossal, and D. L. Sackett. 2003. Stability of drug-induced tubulin rings by fluorescence correlation spectroscopy. *Biochemistry.* 42:1292–1300.
50. Hansen, P. C. 1998. Rank-Deficient and Discrete Ill-Posed Problems. SIAM, Philadelphia, PA.
51. Provencher, S. W. 1992. Low-bias macroscopic analysis of polydispersity. *In* Laser Light Scattering in Biochemistry. S. E. Harding, D. B. Satelle, and V. A. Bloomfield, editors. The Royal Society of Chemistry, Cambridge, UK.
52. Schuck, P. 2000. Size distribution analysis of macromolecules by sedimentation velocity ultracentrifugation and Lamm equation modeling. *Biophys. J.* 78:1606–1619.
53. Eakin, C. M., F. J. Attenello, C. J. Morgan, and A. D. Miranker. 2004. Oligomeric assembly of native-like precursors precedes amyloid formation by β-2 microglobulin. *Biochemistry.* 43:7808–7815.
54. Stojilkoic, K. S., A. M. Berezhkovskii, V. Y. Zitserman, and S. M. Bezrukov. 2003. Conductivity and microviscosity of electrolyte solutions containing polyethylene glycols. *J. Chem. Phys.* 119:6973–6978.
55. Michelman-Ribeiro, A., H. Boukari, R. Nossal, and F. Horkay. 2006. Fluorescence correlation spectroscopy study of TAMRA diffusion in poly(vinyl-alcohol) and Ficoll70 solutions. *Mater. Res. Soc. Symp. Proc.* 897E:J02–J06.
56. Berg, O. G., and P. H. v. Hippel. 1985. Diffusion-controlled macromolecular interactions. *Annu. Rev. Biophys. Biophys. Chem.* 14: 131–160.
57. Chen, Z., P. Earl, J. Americo, I. Damon, S. K. Smith, Y. H. Zhou, F. Yu, A. Sebrell, S. Emerson, G. Cohen, and others. 2006. Chimpanzee/human mAbs to Vaccinia virus B5 protein neutralize Vaccinia and Smallpox viruses and protect mice against Vaccinia virus. *Proc. Natl. Acad. Sci. USA.* 103:1882–1887.
58. Chen, Z., M. Moayeri, Y. H. Zhou, S. Leppla, S. Emerson, A. Sebrell, F. Yu, J. Svitel, P. Schuck, M. St. Claire, and R. Purcell. 2006. Efficient neutralization of anthrax toxin by chimpanzee monoclonal antibodies against protective antigen. *J. Infect. Dis.* 193: 625–633.
59. Vorup-Jensen, T., C. V. Carman, M. Shimaoka, P. Schuck, J. Svitel, and T. A. Springer. 2005. Exposure of acidic residues as a danger signal for recognition of fibrinogen and other macromolecules by integrin $\alpha X\beta 2$. *Proc. Natl. Acad. Sci. USA.* 102:1614–1619.
60. Yarmush, M. L., D. B. Patankar, and D. M. Yarmush. 1996. An analysis of transport resistances in the operation of BIAcore: implications for kinetic studies of biospecific interactions. *Mol. Immunol.* 33:1203–1214.
61. Piehler, J., A. Brecht, K. Hehl, and G. Gauglitz. 1999. Protein interactions in covalently attached dextran layers. *Colloids Surf. B Biointerfaces.* 13:325–336.
62. Fischer, T., M. Beyermann, and K. W. Koch. 2001. Application of different surface plasmon resonance biosensor chips to monitor the interaction of the CaM-binding site of nitric oxide synthase I and calmodulin. *Biochem. Biophys. Res. Commun.* 285: 463–469.
63. Fong, C.-C., M.-S. Wong, W.-F. Fong, and M. Yang. 2002. Effect on hydrogel matrix on binding kinetics of protein-protein interactions on the sensor surface. *Anal. Chim. Acta.* 456:201–208.
64. Parsons, I. D., and P. G. Stockley. 1997. Quantitation of the *Escherichia coli* methionine repressor-operator interaction by surface plasmon resonance is not affected by the presence of a dextran matrix. *Anal. Biochem.* 254:82–87.
65. Karlsson, R., and A. Fält. 1997. Experimental design for kinetic analysis of protein-protein interactions with surface plasmon resonance biosensors. *J. Immunol. Methods.* 200:121–133.
66. Giddings, J. C., E. Kucera, C. P. Russell, and M. N. Myers. 1968. Statistical theory for the equilibrium distribution of rigid molecules in

inert porous networks. Exclusion chromatography. *J. Phys. Chem.* 72:4397–4408.

67. Gorti, S., and B. R. Ware. 1985. Probe diffusion in an aqueous polyelectrolyte solution. *J. Chem. Phys.* 83:6449–6456.
68. Phillies, G. D. J. 1985. Diffusion of bovine serum albumin in a neutral polymer solution. *Biopolymers.* 24:379–386.
69. Crank, J. 1975. The Mathematics of Diffusion. Clarendon Press, Oxford, UK.
70. de Gennes, P. G. 1980. Conformation of polymers attached to an interface. *Macromolecules.* 13:1069–1075.
71. Pero, J. K., E. M. Haas, and N. L. Thompson. 2006. Size dependence of protein diffusion very close to membrane surfaces: measurement by total internal reflection with fluorescence correlation spectroscopy. *J. Phys. Chem. B Condens. Matter Mater. Surf. Interfaces Biophys.* 110:10910–10918.
72. Xu, F., B. Persson, S. Lofas, and W. Knoll. 2006. Surface plasmon optical studies of carboxymethyl dextran brushes versus networks. *Langmuir.* 22:3352–3357.
73. Ramsden, J. J., D. J. Roush, D. S. Gill, R. Kurrat, and R. C. Willson. 1995. Protein adsorption kinetics drastically altered by repositioning a single charge. *J. Am. Chem. Soc.* 117:8511–8516.
74. Zacher, T., and E. Wischerhoff. 2002. Real-time two-wavelength surface plasmon resonance as a tool for the vertical resolution of binding processes in biosensing hydrogels. *Langmuir.* 18:1748–1759.